

Metal surface induces strong acoustic plasmons in chemically doped graphene

Vito Despoja^{1,3,*}, Dino Novko^{1,3}, Ivor Lončarić^{2,3}, Neven Golenić¹, and Vyacheslav M. Silkin^{3,4,5}

¹*Institute of Physics, Bijenička 46, HR-10000 Zagreb, Croatia*

²*Ruder Bošković Institute, Bijenička 54, HR-10000 Zagreb, Croatia*

³*Donostia International Physics Center (DIPC),*

P. Manuel de Lardizabal, 4, 20018 San Sebastián, Spain

⁴*Departamento de Física de Materiales and Centro Mixto CSIC-UPV/EHU, Facultad de Ciencias Químicas, Universidad del País Vasco UPV/EHU, Apto. 1072, 20080 San Sebastián, Spain and*

⁵*IKERBASQUE, Basque Foundation for Science, 48011 Bilbao, Spain*

Recent theoretical considerations have demonstrated that freestanding graphene doped with alkali metals (AC_x) supports strong Dirac and weak acoustic plasmons. Here we show that when AC_x is deposited on a metallic surface, the intense Coulomb screening completely washes out these collective modes. However, even small increase of separation between AC_x and metallic surface causes recovery of AC_x plasmonic properties and especially the enhancement of acoustic plasmons intensities not present in the freestanding case. We further provide the physical background of these intriguing phenomena. The studied systems consist of lithium- and cesium-doped graphene deposited on Ir(111) surface.

I. INTRODUCTION

Ground state crystal and electronic structure of graphene doped with alkali atoms (AC_x , $A = \text{Li, Na, K, Cs}$) on different metallic surfaces, such as Ir(111), Cu(111) and Ni(111), have been recently extensively studied in several experimental and/or theoretical papers [1–7]. The goal of these investigations was to achieve the self-standing graphene (decoupled from the surface as much as possible) with the smallest Moire corrugation. Moreover, the mentioned experiments and further density functional theory (DFT) calculations [8] show that graphene doped by alkali atoms possess electronic band structure that could potentially support very interesting plasmonic properties. On the one hand alkali atoms in two-dimensional (2D) superlattice metalize and form a parabolic σ band that crosses Fermi level [9]. On the other hand, alkali atoms donate electrons to graphene π band, lifting the Fermi level for more than 1 eV above the Dirac point [8]. The coexistence of these partially occupied 2D bands in AC_x could support at least two electronic collective modes, where one is suppose to be very strong Dirac plasmon (DP).

The main goal of this paper is to emphasize very interesting plasmonic effects appearing in graphene doped by alkali metals. Recent theoretical investigations [10, 11] have already pointed out the appearance of a strong DP and a weak acoustic plasmon (AP) [12–14] in AC_x . However, here we focus on much more realistic situation where doped graphene is deposited on metallic surface [15–18] and especially we aim to explore how the vicinity of metallic surface can be exploited to modify the DP and AP dispersion relations and intensities. Investigations of graphene-metal heterostructures is actually of both fundamental [19] and practical [20, 21] importance. For in-

stance, in the field of graphene-based biosensing [21] the graphene-metal contacts are unavoidable and thus deciphering the microscopic screening mechanisms in these structures is of great value.

In this paper we investigate the low-energy collective electronic excitations (2D plasmons) in lithium- and cesium-doped graphene (i.e., LiC_2 and CsC_8) deposited on the Ir(111) surface. The special attention is paid to explore how the vicinity of Ir(111) surface modifies DP and enhances AP intensities. We show how the self-standing doped graphene supports very strong DP and two orders of magnitude weaker AP. When AC_x is at equilibrium separation from the Ir(111) surface, the strong metallic screening destroys the corresponding plasmonics such that the DP in LiC_2 becomes very weak acoustic-like branch, while the DP in CsC_8 almost completely disappears. However, small displacement from the equilibrium separation induces the recovery of plasmon modes as well as the appearance of interesting plasmonic phenomena not present in the freestanding doped graphene. For instance, for displacement of 0.6 – 1.2 Å very strong AP branch appears in LiC_2 and for displacement of 1.2–1.6 Å CsC_8 supports two intense AP modes. For larger wave vectors ($Q > 0.1$ a.u.) the intensities of these APs (laying in infra-red frequency range, $\omega > 1$ eV) can be even two orders of magnitude stronger than the DPs intensities in the self-standing AC_x . These very intriguing plasmonic phenomena can be used in many plasmonics applications [22–31].

In Sec. II A we present theoretical model for the ground state crystal and electronic structure of $\text{LiC}_2/\text{Ir}(111)$ and $\text{CsC}_8/\text{Ir}(111)$. In Sec. II B we present the method for calculating the effective 2D dielectric function $\epsilon(\mathbf{Q}, \omega)$ of $AC_x/\text{Ir}(111)$. In Sec. III the results for electron-energy-loss-spectra (EELS) $-\Im[\epsilon^{-1}]$ and real part of effective 2D dielectric function $\Re[\epsilon]$ in $AC_x/\text{Ir}(111)$ are presented. Finally, we provide the conclusions in Sec. IV.

*Electronic address: vito@phy.hr

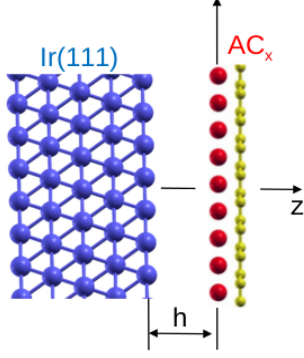


FIG. 1: Crystal structure of alkali atoms doped graphene on Ir(111) surface ($AC_x/\text{Ir}(111)$ composite).

II. THEORETICAL MODEL

A. Ground state

The studied systems consist of graphene doped with alkali atoms and deposited on the Ir(111) surface ($AC_x/\text{Ir}(111)$ composite), as shown in Fig. 1. The separation between alkali atom layer in AC_x and topmost Ir atomic layer of Ir(111) is

$$h = d_{\text{Ir-A}} + \Delta,$$

where $d_{\text{Ir-A}}$ represents the equilibrium separation obtained from DFT calculations and Δ represents the displacement from the equilibrium distance.

The crystal structure of the Ir(111) surface is modeled with 5 atomic layers. Graphene 2×2 superlattice is matched to Ir(111) $\sqrt{3} \times \sqrt{3}$ superlattice such that 4.8% strain is applied to Ir(111). The unit cell in z direction is set to 22 Å.

Ground state electronic and structural optimization calculations were performed using the QUANTUM ESPRESSO (QE) package [32, 33]. The core-electron interaction is approximated by the norm-conserving pseudopotentials [34]. In order to capture the long range van der Waals (vdW) interaction between Ir(111) surface and doped graphene layers we use the vdW exchange correlation functional [35, 36], in particular vdW-DF-cx version [37, 38]. The ground state properties in $AC_x/\text{Ir}(111)$ composites are calculated by using the $9 \times 9 \times 1$ Monkhorst-Pack K-point mesh [39] and the plane-wave cut-off energy is chosen to be 60 Ry. The structural optimization calculations are performed until the maximum force on each atom was reduced below 0.002 eV/Å. The obtained equilibrium separations between different layers in $AC_x/\text{Ir}(111)$ composites are listed in Table I.

B. Calculation of effective 2D dielectric function

Large equilibrium distance $d_{\text{Ir-A}}$ results in small electronic overlap between the AC_x slab and the Ir(111) top-

	LiC ₂	CsC ₈	LiC ₂ /Ir(111)	CsC ₈ /Ir(111)
$d_{\text{Ir-A}}$			2.4	2.97
$d_{\text{A-C}}$	2.17	3.0	1.9	3.17

TABLE I: The equilibrium separations (in Å) between topmost Iridium layer and alkali atoms layer $d_{\text{Ir-A}}$ as well as between alkali atoms layer and graphene layer $d_{\text{A-C}}$ in $AC_x/\text{Ir}(111)$ composite.

most layer which allows us to separate the calculation of the dynamically screened Coulomb interaction into two independent calculations, namely, computation of the AC_x non-interacting electron response function $\chi_{AC_x}^0$ and Ir(111) surface response function D_{Ir} . Such approach considerably reduces the unit cell size and tremendously saves the computational time and memory requirements. This is indeed quite useful for studying the dynamical response in $AC_x/\text{Ir}(111)$ composite when the AC_x - Ir(111) distance is much larger than the equilibrium separation $h \gg d_{\text{Ir-A}}$ or $\Delta \gg 0$.

The ground state electronic structure of LiC₂ and CsC₈ are first calculated using the equilibrium positions $d_{\text{A-C}}$ as in the $AC_x/\text{Ir}(111)$ composite (see Table I) and using other parameters as described in Ref. [40]. The non-interacting electron response functions $\chi_{AC_x}^0$ are calculated using dense K-point grids, i.e., $201 \times 201 \times 1$ and $101 \times 101 \times 1$ K-point meshes for LiC₂ and CsC₈, respectively. The band summations in $\chi_{AC_x}^0$ are performed over 30 and 100 bands, for LiC₂ and CsC₈, respectively. In both cases the damping parameter $\eta = 20$ meV is used. It should be noted here that for response function calculations the crystal local field effects are included only in the perpendicular (z) direction, i.e., the response functions are non-local only in perpendicular direction and can be Fourier transform as $\chi(z, z') = \frac{1}{L} \sum_{G_z G'_z} e^{iG_z z - iG'_z z'} \chi_{G_z G'_z}$ where G_z are reciprocal space vectors in the perpendicular direction. For $\chi_{AC_x}^0$ calculations we use the crystal local field energy cut-off of 10 Ry, which corresponds to 23 G_z wave vectors. The dynamically screened Coulomb interaction can be calculated by solving the Dyson equation $w = v + v \otimes \chi_{AC_x}^0 \otimes w$, where $v = (2\pi/Q)e^{-Q|z-z'|}$ is bare Coulomb interaction [43], and $\otimes \equiv \int_{-\infty}^{\infty} dz$.

In the vicinity of polarizable Ir(111) surface the Coulomb interaction (e.g., interaction between charge density fluctuations at $z, z' > -h$) is mediated by the surface screened Coulomb interaction instead of the bare interaction v

$$w_{\text{Ir}} = v + D_{\text{Ir}} e^{-2Qh} e^{-Q(z+z')},$$

where $D_{\text{Ir}} = \langle e^{Qz_1} | \chi_{\text{Ir}}(\mathbf{Q}, \omega, z_1, z_2) | e^{Qz_2} \rangle$ is the Ir(111) surface response function. The Ir(111) response function χ_{Ir} can be obtained by solving Dyson equation $\chi_{\text{Ir}} = \chi_{\text{Ir}}^0 + \chi_{\text{Ir}}^0 \otimes v \otimes \chi_{\text{Ir}}$, where χ_{Ir}^0 represents the Ir(111) non-interacting electrons response function. The ground state electronic structure of Ir(111)[40] surface is calculated

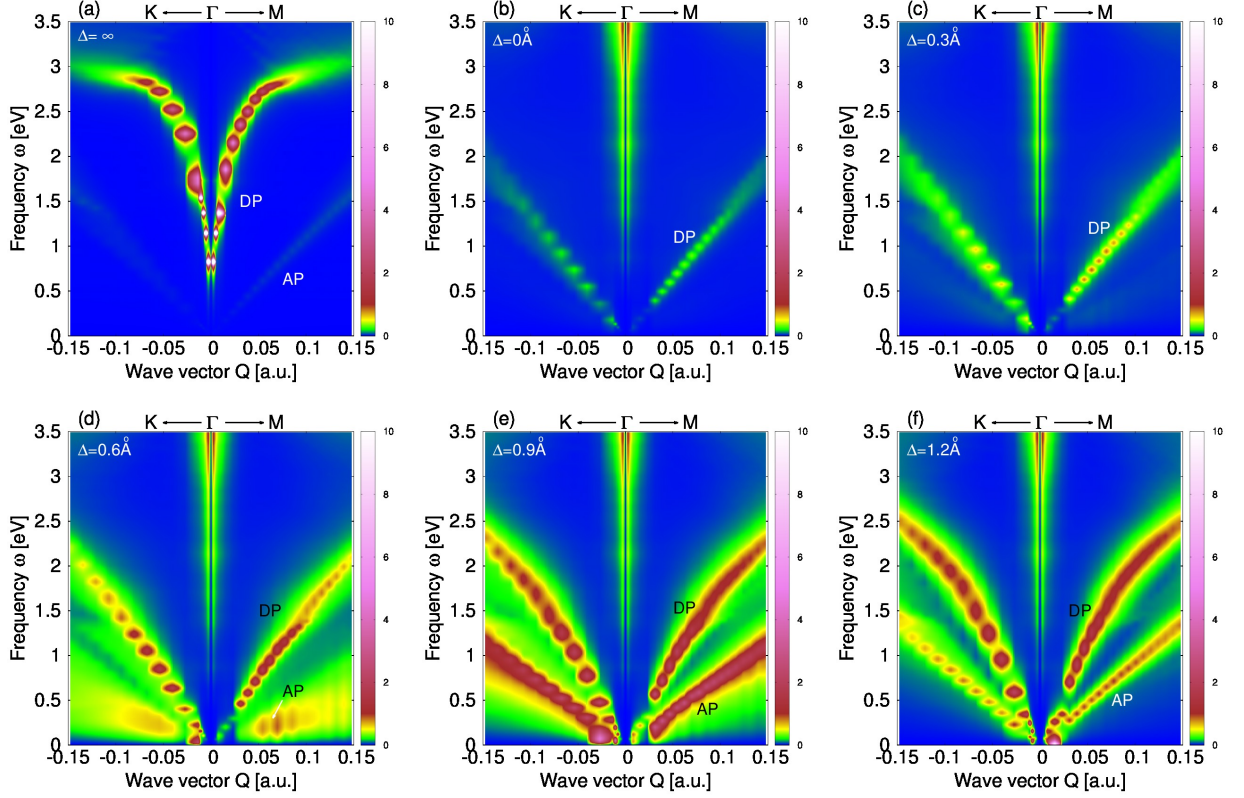


FIG. 2: The EELS intensity in $\text{LiC}_2/\text{Ir}(111)$ composite for (a) $\Delta = \infty$, (b) $\Delta = 0$, (c) $\Delta = 0.3 \text{ \AA}$, (d) $\Delta = 0.6 \text{ \AA}$, (e) $\Delta = 0.9 \text{ \AA}$, and (f) $\Delta = 1.2 \text{ \AA}$.

using the 1×1 unit cell. The response function χ_{Ir}^0 is calculated using $101 \times 101 \times 1$ K-point mesh and the band summations is performed over 150 bands. The damping parameter $\eta = 30 \text{ meV}$ is used. The crystal local field energy cut of 10 Ry is used, which equal to the $37 G_z$ wave vectors.

After the AC_x is deposited on the polarizable $\text{Ir}(111)$ surface the bare Coulomb interaction v has to be replaced by the surface screened Coulomb interaction ($v \rightarrow w_{\text{Ir}}$) and the dynamically screened Coulomb interaction of the entire $\text{AC}_x/\text{Ir}(111)$ composite is calculated by solving the “screened” Dyson equation:

$$w = w_{\text{Ir}} + w_{\text{Ir}} \otimes \chi_{\text{AC}_x}^0 \otimes w. \quad (1)$$

Finally, the effective 2D dielectric function can be defined as

$$\epsilon^{-1}(\mathbf{Q}, \omega) = w(\mathbf{Q}, \omega, z=0, z'=0)/v_Q,$$

where $v_Q = 2\pi/Q$. The EELS is then calculated as $S(\mathbf{Q}, \omega) = -(1/\pi)\Im[\epsilon^{-1}(\mathbf{Q}, \omega)]$.

III. RESULTS AND DISCUSSION

We shall first describe the modifications obtained in the electronic excitation spectra of AC_x when it is

brought from self-standing ($\Delta \rightarrow \infty$) to equilibrium ($\Delta = 0$) distance. In addition, we shall gradually increase the separation $\Delta > 0$, present the corresponding spectra and explain the physical background of the spectral alterations.

Figure 2(a) shows the EELS intensity in self-standing ($\Delta = \infty$) LiC_2 . As already reported in Ref. [10] in LiC_2 Li atoms donate electrons to graphene π^* band and at the same time they metalize and form parabolic σ band which remains partially filled. Therefore, there are two bands crossing Fermi level which result in two plasmons in LiC_2 , i.e., strong DP and weak AP [see Fig. 2(a)]. Figure 2(b) shows EELS intensities in LiC_2 when it is at the equilibrium distance ($\Delta = 0$) from the $\text{Ir}(111)$ surface. It turns out that metallic surface radically modifies the intensities of the electronic modes in LiC_2 . Namely, the DP becomes very weak and changes to a linearly dispersive mode, while the AP disappears. Strong metallic screening obviously significantly reduces the intensity of electronic modes and pushes them toward lower energies. In order to verify this claim in Figs. 2(c)-(e) we show the EELS spectra of LiC_2 , where the separation between LiC_2 and $\text{Ir}(111)$ is gradually increased, from $\Delta = 0.3 \text{ \AA}$ to $\Delta = 1.2 \text{ \AA}$. Figure 2(c) shows that even small displacement of $\Delta = 0.3 \text{ \AA}$ from equilibrium causes substantial increase of DP intensity, while the dispersion remains linear. For $\Delta = 0.6 \text{ \AA}$ shown in Fig. 2(d) the

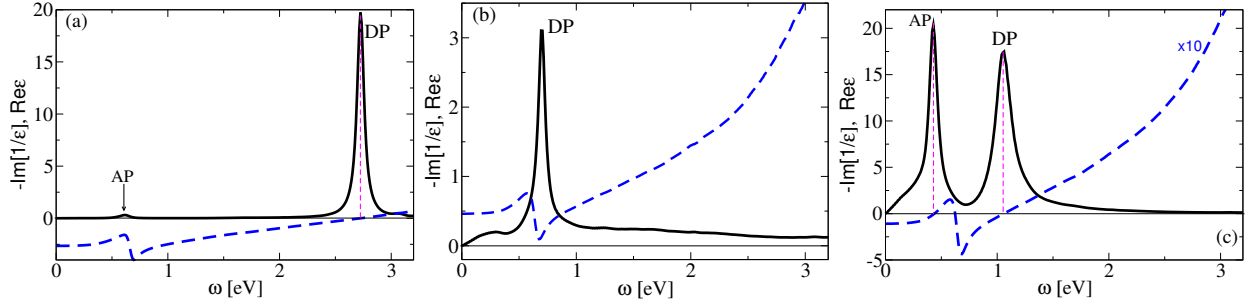


FIG. 3: The EELS (black solid) and $\Re[\epsilon]$ (blue dashed) in $\text{LiC}_2/\text{Ir}(111)$ composite for (a) $\Delta = \infty$, (b) $\Delta = 0$, and (c) $\Delta = 0.9 \text{ \AA}$. The transfer wave vector of magnitude $Q = 0.054 \text{ a.u.}$ is chosen to be in Γ -M direction.

broad AP appears in the lower energy region and the DP becomes stronger. Already for this separation the intensity of AP is an order of magnitude stronger than the intensity of the AP in the self-standing LiC_2 [see Fig 2(a)]. For $\Delta = 0.9 \text{ \AA}$ shown in Fig. 2(e) the dispersion relation of the DP bends (i.e., it is no longer linear) and its energy and intensity increase. The AP becomes strong, sharp and well defined plasmon mode with intensity two orders of magnitude larger than in self-standing LiC_2 and even stronger than the corresponding DP. For $\Delta = 1.2 \text{ \AA}$, shown in Fig. 2(f), the AP intensity reduces for an order of magnitude (in comparison with the $\Delta = 0.9 \text{ \AA}$ case) and the intensity of DP continues to increase toward its self-standing ($\Delta = \infty$) value. It is important to note that since the metallic screening reduces the plasmon frequency, it pushes the DP out of the interband $\pi \rightarrow \pi^*$ continuum [44], which in turn reduces the Landau damping and increases the intensity of the plasmon compared to the self-standing case (e.g., compare the intensities in Figs. 2(e) and 2(f) with the intensities in Fig. 2(a) when $Q > 0.1 \text{ a.u.}$). Also, we note that for the shown wave-vector interval the EELS intensities are almost isotropic, i.e. $S(\mathbf{Q}_{\Gamma\text{M}}, \omega) \approx S(\mathbf{Q}_{\Gamma\text{K}}, \omega)$.

The panels in Fig. 2 clearly show that when $\text{LiC}_2 - \text{Ir}(111)$ distance is out of equilibrium $\Delta > 0$, the $\text{Ir}(111)$ surface induces the strong AP but only for small interval of separations $0.5 < \Delta < 1.0 \text{ \AA}$. In order to clarify this phenomenon we show in Fig. 3 the real part of the effective 2D dielectric function (blue dashed lines) for three characteristic separations (a) $\Delta = \infty$, (b) $\Delta = 0$, and (c) $\Delta = 0.9 \text{ \AA}$ and for $Q = 0.054 \text{ a.u.}$ in the Γ -M direction. The corresponding EELS are shown by black solid lines. It can be seen that in all of the cases the $\Re[\epsilon]$ contains “kink” structures which, depending on separation from the $\text{Ir}(111)$ surface, shifts up and down as well as crosses zero at different frequencies. For $\Delta = \infty$ the “kink”, where the weak AP appears, is entirely below zero. At the higher frequencies, i.e., after the “kink”, the $\Re[\epsilon]$ increases and crosses the zero where strong DP appears, classifying the DP as a well-defined collective electronic mode. On the other hand, when $\Delta = 0$ the “kink” is entirely above the zero and $\Re[\epsilon]$ does not cross the zero at all. This results in the appearance of the weak DP around the dip of $\Re[\epsilon]$. Considering that when $\Delta = \infty$

changes to $\Delta = 0$ the “kink” in $\Re[\epsilon]$ transforms from entirely below to entirely above the zero, there should be some Δ interval when the “kink” crosses zero. As can be seen from Fig. 3(c) this situation occurs, e.g., when $\Delta = 0.9 \text{ \AA}$ resulting in the appearance of AP and DP. In that case both plasmons can be classified as strong well-defined collective modes, as is obvious from Fig. 2(e). For slightly larger separation, i.e., $\Delta > 1.0$, the “kink” falls entirely below the zero and the AP quickly weakens. However, $\Re[\epsilon]$ continues to cross zero at larger frequencies where strong DP appears, as is also obvious from Fig. 2(f).

Further, we show the EELS intensity of the self-standing ($\Delta = \infty$) CsC_8 in Fig. 4(a). In CsC_8 the graphene π^* band crosses Fermi level twice which together with partially filled parabolic $\text{Cs}(\sigma)$ band [11] is sufficient for the appearance of the three plasmons, i.e., the strong DP and the two weak acoustic plasmons, which we dub AP_1 and AP_2 . This nomenclature for acoustic plasmons is just formal since their dispersion will not be necessary linear. Figure 4(b) shows the EELS intensity in CsC_8 when it is at equilibrium distance ($\Delta = 0$) from the $\text{Ir}(111)$ surface. The strong metallic screening extremely weakens the oscillatory strengths of the electronic modes such that the DP and AP_2 become weak and barely visible modes, while the AP_1 disappears. Figures 4(c)-(e) show the EELS intensities in CsC_8 when the separation between CsC_8 and $\text{Ir}(111)$ surface gradually increases, from $\Delta = 0.4 \text{ \AA}$ to $\Delta = 1.6 \text{ \AA}$. For $\Delta = 0.4 \text{ \AA}$ shown in Fig. 4(c) the EELS intensity slightly increases, however, for $\Delta = 0.8 \text{ \AA}$ shown in Fig. 4(d) the enhancement of the EELS intensity is already significant and new AP_1 plasmon appears. It can be noticed that AP_1 and AP_2 have square-root dispersions, which is especially visible in Γ -M direction. In Γ -K direction, the AP_1 is still very broad emerging mode. For $\Delta = 1.2 \text{ \AA}$ shown in Fig. 4(e) the AP_1 and AP_2 turn out to be strong well-defined plasmon modes. In Γ -K direction the AP_1 and AP_2 have well separated dispersion relations, while in Γ -M direction and for larger wave vectors $Q > 0.1 \text{ a.u.}$ these modes are degenerate. Interesting feature occurs in long-wavelength limit $Q \approx 0$, especially in Γ -M direction, where AP_2 and DP start as a one plasmon branch and then at $Q \approx 0.025 \text{ a.u.}$ they bifurcate, i.e., the DP

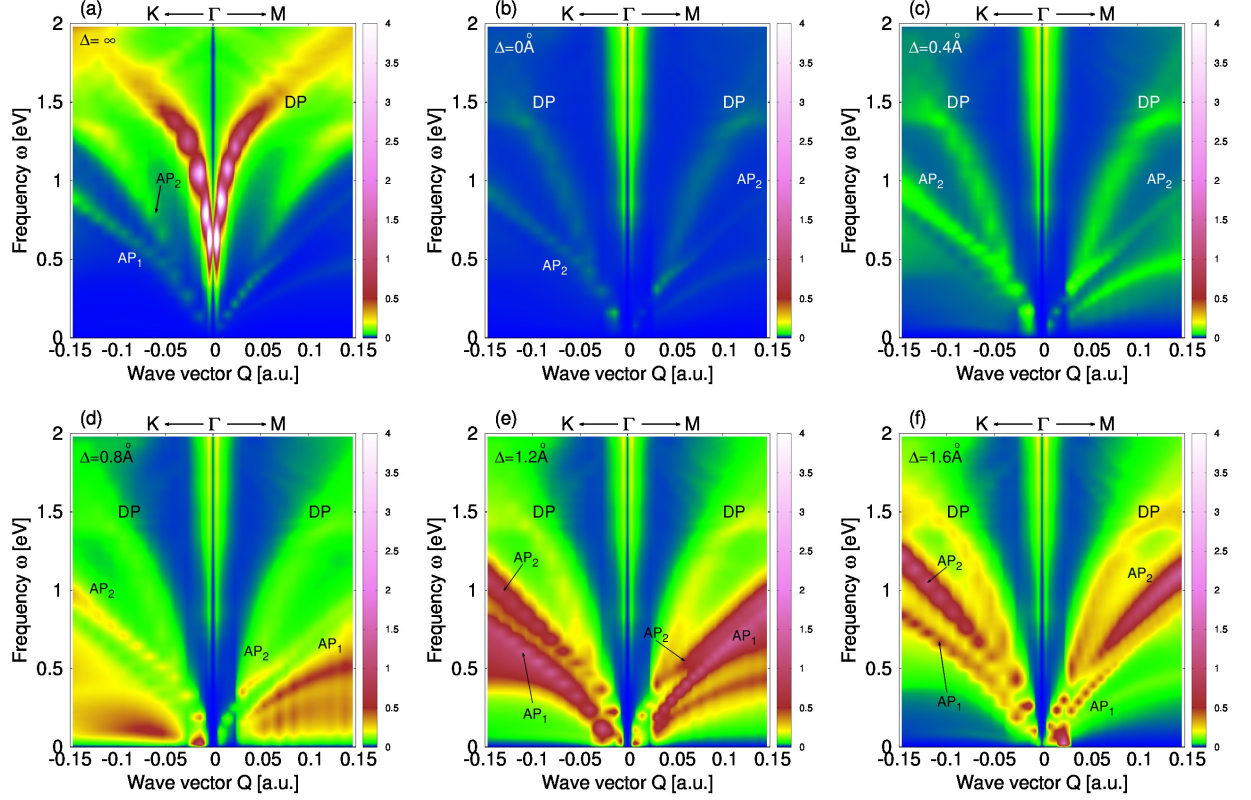


FIG. 4: The EELS intensity in CsC₈/Ir(111) composite for (a) $\Delta = \infty$, (b) $\Delta = 0$, (c) $\Delta = 0.4 \text{ \AA}$, (d) $\Delta = 0.8 \text{ \AA}$, (e) $\Delta = 1.2 \text{ \AA}$, and (f) $\Delta = 1.6 \text{ \AA}$.

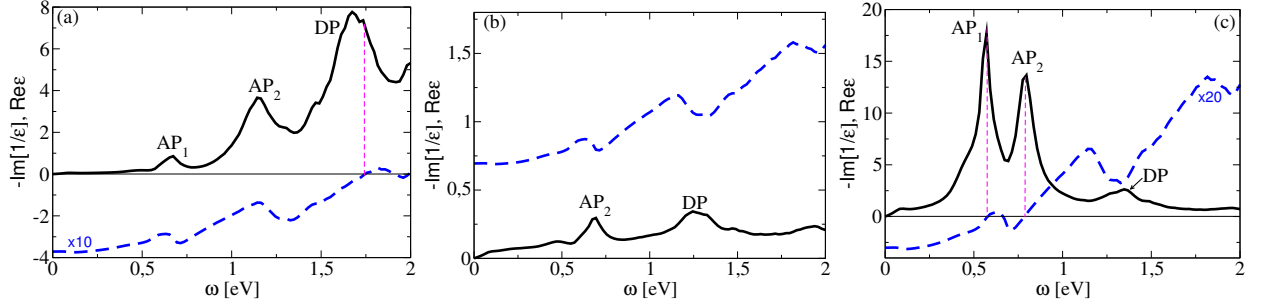


FIG. 5: The EELS (black solid) and $\Re[\epsilon]$ (blue dashed) in CsC₈/Ir(111) composite for (a) $\Delta = \infty$, (b) $\Delta = 0$, and (c) $\Delta = 1.3 \text{ \AA}$. The transfer wave vector of magnitude $Q = 0.094 \text{ a.u.}$ is chosen to be in Γ -K direction.

continues as square-root and AP₂ as linear branches. For $\Delta = 1.6 \text{ \AA}$ shown in Fig. 4(f) the AP₁ is already notably weakened, the AP₂ is still very strong mode, especially for larger wave vectors $Q > 0.1 \text{ a.u.}$ in both (Γ -M and Γ -K) directions, while the DP continues to strengthen. The observable bifurcation into AP₂ and DP branches is still present, in both directions for $Q \approx 0.05 \text{ a.u.}$ As already discussed, in the LiC₂ case, for $\Delta > 2 \text{ \AA}$ the AP₁ and AP₂ suddenly weaken and DP becomes gradually stronger until its intensity reaches the freestanding ($\Delta = \infty$) value.

In order to understand the appearance of the strong acoustic plasmons AP₁ and AP₂ in CsC₈ for certain sep-

arations Δ , in the panels of Fig. 5 we show the real parts (blue dashed lines) of the effective 2D dielectric function ($\Re[\epsilon]$) for three characteristic separations (a) $\Delta = \infty$, (b) $\Delta = 0$ and (c) $\Delta = 1.3 \text{ \AA}$, and for $Q = 0.094 \text{ a.u.}$ in the Γ -K direction. The EELS are shown by the black solid lines. Contrary to the LiC₂ case, it can be seen that the $\Re[\epsilon]$ of CsC₈ has two “kinks” which move up and down depending on the separation Δ . This means that for certain separations Δ the $\Re[\epsilon]$ can cross zero three times, and, therefore, three well-defined plasmons appear. Figure 5(a) shows that both “kinks” are entirely below zero, which gives only weak plasmons. For larger frequencies, after the “kink” structures, the $\Re[\epsilon]$ crosses zero provid-

ing relatively strong, but quite broad DP. This is reasonable considering that for this wave vector the DP already enters $\pi \rightarrow \pi^*$ interband continuum and is thus considerably Landau damped[44]. This effect can also be seen as sudden decrease of DP intensity for $Q > 0.05$ a.u. in Fig. 4(a). For $\Delta = 0$ the “kinks” are entirely above the zero and $\Re[\epsilon]$ does not cross the zero at all. This results in only two very weak plasmons AP_2 and DP around where the dips of the “kink” structures appear. Mapping the conclusions from the LiC_2 case, we expect a narrow Δ interval as well for the CsC_8 where at least one of the “kinks” crosses zero. It should also be noted that for this system there is no Δ for which both “kinks” would cross zero simultaneously. Figure 5(c) shows that for $\Delta = 1.3$ Å the first “kink” crosses zero two times which results in strong and well-defined plasmons AP_1 and AP_2 . The second “kink” is still above zero resulting in a weak DP just below the dip in the “kink”. This corresponds to the situation shown in Fig. 4(e) where the two strong plasmon, i.e., AP_1 and AP_2 , and the weak DP bands are present. It is important to note here that for $\Delta = 1.3$ Å [Fig. 5(c)] the intensities of AP_1 and AP_2 are an order of magnitude larger than AP_1 and AP_2 intensities and more than two times larger than DP intensity in CsC_8 for equilibrium separation $\Delta = 0$ [Fig. 5(c)], at the same wave vector Q . For slightly larger $\Delta > 2.0$ Å both “kinks” fall below the zero and AP_1 and AP_2 quickly weaken, however the $\Re[\epsilon]$ continues to cross zero for larger frequencies where stronger DP is present (not shown).

These results generally show that for narrow interval of displacements [i.e., $0.5 \text{ Å} \leq \Delta \leq 1.0 \text{ Å}$ for $LiC_2/Ir(111)$ and $1.0 \text{ Å} \leq \Delta \leq 1.5 \text{ Å}$ for $CsC_8/Ir(111)$] the $AC_x/Ir(111)$ composites support strong APs which are for small wave vectors (i.e., $Q < 0.05$ a.u.) as strong as the DP in the self-standing cases. These APs persist as strong well-defined collective modes in the wide wave vector interval (i.e., $0 < Q < 0.15$ a.u.) such that for larger wave vectors ($Q > 0.1$ a.u.) APs may be even three orders of magnitude stronger [see Figs. 2(e)-(f) and Figs. 4(e)-(f)] than the Landau damped DPs in self-standing systems [see Fig. 2(a) and Fig. 4(a)]. The metallic screening pushes the DP towards lower frequencies such that in the $LiC_2/Ir(111)$ composite DP leaves the interband $\pi \rightarrow \pi^*$ continuum and becomes sharp long-lived mode. Achieving these very interesting plasmonic features requires an artificial ejection of the $AC_x/Ir(111)$ from the equilibrium distance Δ which might be experimentally feasible. For instance, by placing the inert single or few layers of hexagonal boron-nitride between graphene and metal surface, as it is actually the case in the contemporary graphene-based devices [19, 20]. Or by replacing the alkali atoms by more larger intercalants, such as the $FeCl_3$ molecules that act as the electron acceptors lowering the Fermi energy below -1 eV [45]. Furthermore, the desirable plasmonic properties could be even achieved by changing the concept of the composite system. For example, instead of using metallic substrate

we can use semiconducting (e.g., SiO_2) substrates, while the plasmonic properties in AC_x /substrate could be manipulated by the dull metallic (e.g., aluminum) tip from the above.

IV. CONCLUSIONS

We have demonstrated how the 2D collective modes in chemically doped graphene are drastically modified in the presence of the $Ir(111)$ metallic surface. For instance, very strong Dirac plasmon present in LiC_2 becomes two order of magnitude weaker and linearly dispersive, while the acoustic plasmon disappears. Similar modifications were as well observed in CsC_8 . Further, to understand this physical phenomena we gradually increased the graphene-surface separations Δ and analyzed the effective 2D dielectric function ϵ . We have found that for the equilibrium separation ($\Delta = 0$) the strong metallic screening pushes the real part of effective 2D dielectric function ($\Re[\epsilon]$) entirely above the zero which blocks the formation of well-defined 2D collective modes. However, for narrow interval of out-of-equilibrium separations ($\Delta > 0$) the $\Re[\epsilon]$ crosses zero twice providing two strong 2D plasmons. In particular, for $0.5 \text{ Å} \leq \Delta \leq 1.0 \text{ Å}$ the $LiC_2/Ir(111)$ composite supports strong well-defined Dirac and acoustic plasmons, while for $1.0 \text{ Å} \leq \Delta \leq 1.5 \text{ Å}$ the $CsC_8/Ir(111)$ composite contains two intense acoustic plasmons when the wave vector is smaller than 0.15 a.u. All in all, we have shown that the chemically doped graphene in the presence of the metallic surface could support even superior plasmonic features compared to the freestanding case. This manipulative plasmonic property can be used in many applications such as biosensing or in plasmon enhanced spectroscopic techniques.

Acknowledgment

V.D. acknowledges support from the QuantiXLie Center of Excellence, a project cofinanced by the Croatian Government and European Union through the European Regional Development Fund - the Competitiveness and Cohesion Operational Programme (Grant No. KK.01.1.1.01.0004). V.D. is also grateful to Donostia International Physics Center (DIPC) for hospitality during various stages of this work. D.N. acknowledges financial support from the European Regional Development Fund for the “Center of Excellence for Advanced Materials and Sensing Devices” (Grant No. KK.01.1.1.01.0001). I.L. acknowledges support from the European Union through the European Regional Development Fund - the Competitiveness and Cohesion Operational Programme (KK.01.1.1.06). Computational resources were provided by the DIPC Computing Center.

-
- [1] P. Pervan, P. Lazić, M. Petrović, I. Šrut Rakić, I. Pletikosić, M. Kralj, M. Milun, and T. Valla Phys. Rev. B **92**, 245415 (2015)
- [2] J. Halle, N. Neel and J. Kroger, Phys. Chem. C **120**, 5067 (2016)
- [3] M. Petrović, I. Šrut Rakić, S. Runte, C. Busse, J. T. Sadowski, P. Lazić, I. Pletikosić, Z.-H. Pan, M. Milun, P. Pervan, N. Atodiressei, R. Brako, D. Šokčević, T. Valla, T. Michely and M. Kralj, Nature Commun. **4**, 2772 (2013)
- [4] S. Tanaka, M. Petrović, K. Watanabe, P. Lazić, M. Kralj, T. Sugimoto and Y. Matsumoto, *Excitation of surface plasmons in highly-doped graphene by visible light*, under review.
- [5] S. Schumacher, T. Wehling, P. Lazić, S. Runte, D. F. Forster, C. Busse, M. Petrović, M. Kralj, S. Blugel, N. Atodiressei, V. Caciuc, and T. Michely, Nano Lett. **13**, 5013 (2013)
- [6] B. Cook, A. Russakoff, and K. Varga, Appl. Phys. Lett. **106**, 211601 (2015);
- [7] M. Alattas and U. Schwingenschlogl, Scientific Reports **6**, 26753 (2016)
- [8] D. Novko, Dopant-induced plasmon decay in graphene, Nano Lett., **17**, 6991 (2017)
- [9] I. Lončarić, Z. Rukelj, V. M. Silkin, V. Despoja, npj 2D Materials and Applications, **2**, 33 (2018)
- [10] L. Marušić and V. Despoja, Phys. Rev. B **95** (2017) 201408(R)
- [11] V. Despoja and L. Marušić, Phys. Rev. B **97** (2018) 205426
- [12] J. M. Pitarke, V. U. Nazarov, V. M. Silkin, E. V. Chulkov, E. Zaremba, and P. M. Echenique, Phys. Rev. B **70**, 205403 (2004)
- [13] B. Diaconescu, K. Pohl, L. Vattuone, L. Savio, P. Hofmann, V. M. Silkin, J. M. Pitarke, E. V. Chulkov, P. M. Echenique, D. Farías and M. Rocca, Nature **448**, 57 (2007)
- [14] V. M. Silkin, J. M. Pitarke, E. V. Chulkov, B. Diaconescu, K. Pohl, L. Vattuone, L. Savio, Ph. Hofmann, D. Farías, M. Rocca, and P. M. Echenique, Phys. Stat. Sol. **205**, 1307 (2008)
- [15] T. Langer, D. F. Forster, C. Busse, T. Michely, H. Pfnir and C. Tegenkamp, New Journal of Physics **13**, 053006 (2011)
- [16] A. Politano, H. K. Yu, D. Farías and G. Chiarello, Phys. Rev B **97**, 035414 (2018)
- [17] A. Principi, E. van Loon, M. Polini, and M. I. Katsnelson, Phys. Rev. B **98**, 035427 (2018)
- [18] A. R. Echarri, Joel D. Cox, and F. J. G. de Abajo, Optica **6**, 630 (2019)
- [19] M. B. Lundeborg, Y. Gao, R. Asgari, et al., Science **357**, 187 (2017)
- [20] D. A. Iranzo, S. Nanot, E. J. C. Dias, et al., Science **360**, 291 (2018)
- [21] D. Rodrigo, O. Limaj, D. Janner, et al., Science **349**, 165 (2015)
- [22] M. Pumera, Materialstoday **14**, 308 (2011)
- [23] E. Singh, M. Meyyappan and H. S. Nalwa, ACS Appl. Mater. Interfaces **9** (40), 34544 (2017)
- [24] T. Mahmoudi, Y. Wang, Yoon-Bong Hahn, Nano Energy **47**, 51 (2018)
- [25] Y. Miyoshi, Y. Fukazawa, Y. Amasaka, R. Reckmann, T. Yokoi, K. Ishida, K. Kawahara, H. Ago and H. Maki, Nature Communications **9**, 279 (2018)
- [26] T. Low and P. Avouris, ACS Nano **8**, 1086 (2014)
- [27] S. Huang, C. Song, G. Zhang and H. Yan, Nanophotonics **6**, 1191 (2017)
- [28] M. Jablan, H. Buljan, M. Soljačić, Phys. Rev. B **80**, 245435 (2009),
- [29] K.S. Novoselov, V. I. Falko, L. Colombo, P.R. Gellert, M. G. Schwab, K. Kim, Nature **490**, 192 (2012); F. Schwierz, Proc. IEEE **101** 1567 (2013); F. Xia, Proc. IEEE **101**, 1717 (2013).
- [30] M. Jablan, M. Soljačić, H. Buljan, Proceedings of the IEEE **101**, 1689 (2013)
- [31] S. Xiao, X. Zhu, Bo-Hong Li, N. Asger Mortensen, Front. Phys. **11**, 117801 (2016)
- [32] P. Giannozzi, S. Baroni, N. Bonini, M. Calandra, R. Car, C. Cavazzoni, D. Ceresoli, G. L. Chiarotti, M. Cococcioni, I. Dabo, et al., J. Phys.: Condens. Matter **21**, 395502 (2009)
- [33] P. Giannozzi, O. Andreussi, T. Brumme, O. Bunau, M. Buongiorno Nardelli, M. Calandra, R. Car, C. Cavazzoni, D. Ceresoli, M. Cococcioni, et al., J. Phys.: Condens. Matter **29**, 465901 (2017)
- [34] N. Troullier and J. L. Martins, Phys. Rev. B **43**, 1993 (1991)
- [35] I. Lončarić, V. Despoja, Phys. Rev. B **90**, 075414 (2014)
- [36] C. Busse et al., Phys. Rev. Lett. **107**, 036101 (2011)
- [37] K. Berland, et al., J. Chem. Phys. **140**, 18A539 (2014).
- [38] P. Hyldgaard, K. Berland and E. Schroder, Phys. Rev. B **90**, 075148 (2014).
- [39] H.J. Monkhorst and J.D. Pack, Phys. Rev. B **13**, 5188 (1976)
- [40] DFT calculations of separate layers are performed in the same way as for the complete system, except XC potential in LiC₂ is approximated by the Perdew-Zunger local density approximation (LDA) [41] and in CsC₈ and Ir(111) surface by Perdew-Burke-Ernzerhof generalized gradient approximations (GGA)[42]. We used $12 \times 12 \times 1$, $6 \times 6 \times 1$ and $12 \times 12 \times 1$ Monkhorst-Pack K-point mesh for LiC₂, CsC₈, and Ir(111), respectively. Supercells in z direction for AC_{*x*} are set to 12.3 Å and for Ir(111) surface to 20.9 Å.
- [41] J.P. Perdew and A. Zunger, Phys. Rev. B **23**, 5048 (1981)
- [42] J.P. Perdew, K. Burke, and M. Ernzerhof, Phys. Rev. Lett. **77**, 3865 (1996)
- [43] V. Despoja, Z. Rukelj and L. Marušić, Phys. Rev. B **94**, 165446 (2016)
- [44] V. Despoja, D. Novko, K. Dekanić, M. Sunjić and L. Marušić, Phys. Rev. B **87**, 075447 (2013)
- [45] F. J. Bezares, A. De Sanctis J. R. M. Saavedra, et al., Nano Lett. **17**, 5908 (2017)